Nuclear Instruments and Methods in Physics Research A 689 (2012) 12–21

Contents lists available at SciVerse ScienceDirect

Nuclear Instruments and Methods in Physics Research A

journal homepage: www.elsevier.com/locate/nima

The Dexela 2923 CMOS X-ray detector: A flat panel detector based on CMOS active pixel sensors for medical imaging applications

Anastasios C. Konstantinidis *, Magdalena B. Szafraniec, Robert D. Speller, Alessandro Olivo

Department of Medical Physics and Bioengineering, Malet Place Engineering Building, University College London, Gower Street, London, WC1E 6BT, UK

ARTICLE INFO

Article history:
Received 22 March 2012
Received in revised form
12 June 2012
Accepted 18 June 2012
Available online 26 June 2012

Keywords:
CMOS APS
Digital X-ray detector
Mammography
Radiography
DQE

ABSTRACT

Complementary metal-oxide-semiconductors (CMOS) active pixel sensors (APS) have been introduced recently in many scientific applications. This work reports on the performance (in terms of signal and noise transfer) of an X-ray detector that uses a novel CMOS APS which was developed for medical X-ray imaging applications. For a full evaluation of the detector's performance, electro-optical and X-ray characterizations were carried out. The former included measuring read noise, full well capacity and dynamic range. The latter, which included measuring X-ray sensitivity, presampling modulation transfer function (pMTF), noise power spectrum (NPS) and the resulting detective quantum efficiency (DQE), was assessed under three beam qualities (28 kV, 50 kV (RQA3) and 70 kV (RQA5) using W/Al) all in accordance with the IEC standard. The detector features an in-pixel option for switching the full well capacity between two distinct modes, high full well (HFW) and low full well (LFW). Two structured CsI:Tl scintillators of different thickness (a "thin" one for high resolution and a thicker one for high light efficiency) were optically coupled to the sensor array to optimize the performance of the system for different medical applications. The electro-optical performance evaluation of the sensor results in relatively high read noise ($\sim$360 e^-), high full well capacity ($\sim 1.5\times10^6$ e^-) and wide dynamic range ($\sim$73 dB) under HFW mode operation. When the LFW mode is used, the read noise is lower ($\sim$165) at the expense of a reduced full well capacity ($\sim 0.5\times10^6$ e^-) and dynamic range ($\sim$69 dB). The maximum DQE values at low frequencies (i.e. 0.5 lp/mm) are high for both HFW (0.69 for 28 kV, 0.71 for 50 kV and 0.75 for 70 kV) and LFW (0.69 for 28 kV and 0.7 for 50 kV) modes. The X-ray performance of the studied detector compares well to that of other mammography and general radiography systems, obtained under similar experimental conditions. This demonstrates the suitability of the detector for both mammography and general radiography, with the use of appropriate scintillators. The high DQE values obtained under low mammographic exposures (up to 0.65 for 22.3 μGy) matches the demand for high detectability in imaging of the dense breast.

1. Introduction

Complementary metal-oxide-semiconductors (CMOS) active pixel sensors (APS) have been introduced recently in medical X-ray imaging [1–5]. These sensors integrate the signal and operate by resetting the photoelement (usually a photodiode) in each pixel, allowing charge to accumulate and finally sensing the charge value. The term "active" indicates, at the minimum, the presence of a source follower transistor in each pixel, which buffers and/or amplifies the accumulated signal [6]. Therefore, the signal is transferred onto a common readout bus as voltage rather than charge, improving the sensor's signal-to-noise ratio (SNR) and readout speed.

In the last twenty years charged coupled devices (CCD) and active matrix flat panel imagers (AMFPI; also known as thin film transistors (TFT)) have been the workhorse in medical X-ray imaging [7–12]. However, the production cost of CCDs is high and their active area is limited to about 4 cm^2 [13]. Therefore, it is often necessary to demagnify the image from the scintillator to allow coverage of the required X-ray field size in the patient. There are three ways to demagnify the light signal: using optical lenses, fiber optic tapers (FOT), or electron-optic coupling [11]. However, this demagnification stage increases the quantum sink by imposing stricter requirements on light propagation in order to keep image quality within acceptable levels [14]. CCDs are also susceptible to radiation damage [15,16]. These are the main

* Corresponding author.
E-mail addresses: a.konstantinidis@medphys.ucl.ac.uk, taskon25@yahoo.gr (A.C. Konstantinidis).

0168-9002/$ - see front matter © 2012 Elsevier B.V. All rights reserved.
http://dx.doi.org/10.1016/j.nima.2012.06.024

reasons why, over recent years, AMFPIs have become the detector of choice in mammography and general radiography. AMFPIs are high-performing detectors; however, margins of improvements may still exist in some areas. For example, in tomosynthesis and fluoroscopy, where limitations on patient dose impose a small exposure per frame, reduced detection quantum efficiency (DQE) at low exposure levels has been reported for AMFPIs by some authors [17–19]. This has been attributed primarily to high read noise due to the use of passive pixels [20–22]. Other authors have reported problems related to image lag, ghosting and baseline drifts [23,24]. These however will not be investigated in the present paper, which deals primarily with electro-optical and X-ray characterization, and might be the subject of future investigations.

CMOS sensors have the potential for low-cost mass production and low power consumption which could offer an alternative. Stitching and tiling technologies can be used to obtain large area sensors suitable for medical X-ray applications [22,25,26]. Radiation tolerant CMOS sensors have already been presented [27,28]. Moreover, CMOS sensors offer very fast image acquisition [29,30] and low read noise at high-frame-rates due to column parallel read out [16]. Finally, the CMOS APS features lower read noise than passive pixel sensors (PPS) [5,13] due to the presence of the source follower in each pixel.

The X-ray detector under investigation consists of a photodiode array with a 75 μm pixel pitch, and it has been developed primarily for medical X-ray imaging applications [31]. The detector is capable of multi-resolution readout with pixels binned 1×2, 2×2, 1×4, 2×4 and 4×4 allowing the frame rate to range from 26 frames per second (fps) at full resolution, to 86 fps in 4×4 binning mode over the entire active area. Also, this detector features an option for switching the full well capacity between two separate levels, named high full well (HFW) and low full well (LFW) modes. This paper evaluates both the electro-optical and X-ray performance of the detector. The electro-optical performance, which includes read noise, full well capacity and dynamic range, has been evaluated using mean-variance (MV) analysis. The X-ray performance has been quantified under three beam qualities all in accordance with the IEC standard [32,33], using metrics such as X-ray sensitivity, presampling modulation transfer function (pMTF), noise power spectrum (NPS) and detective quantum efficiency (DQE). These measurements were performed under mammographic and general radiography conditions.

2. Materials and methods

2.1. The CMOS X-ray detector developed by Dexela

The CMOS X-ray detector developed by Dexela Limited (a PerkinElmer company). The basic design of the pixel is based on the standard APS architecture [29,34]. However, each pixel contains an extra feature, i.e. an option for switching the full well capacity of the pixel between two separate modes, namely high full well (HFW) and low full well (LFW). This feature is operated globally across the whole active area and statically. The LFW mode has lower read noise in both unbinned and binned modes. This increases the detector sensitivity at low Air Kerma (K_a) levels. In other words, the LFW mode has lower full well capacity but is more sensitive. It has been designed for high DQE values at low K_a levels [31].

The typical active area of a single sensor module at full resolution (pixel pitch equal to 75 μm) is 1944×1536 pixels, i.e. 11.5×14.5 cm^2. Each sensor has six parallel readout channels using stitching technology [22,25,26]. Sensors can be tiled in a two dimensional (2D) array to obtain larger fields of view suitable for a variety of medical applications. The X-ray detector under investigation is a 2×2 array (3888×3072 pixels) with an overall area of 29×23 cm^2, and is intended for use in mammography, breast tomosynthesis, cone beam computed tomography (CBCT) and fluoroscopy. The binning capability allows a trade-off between spatial and temporal resolutions. The 75 μm pixel resolution allows a frame rate of 26 fps, while the 300 μm resolution (4×4 binning mode) corresponds to a maximum rate of 86 fps which is suitable for dynamic applications.

2.2. Electro-optical performance evaluation

2.2.1. Sensor performance parameters

Electro-optical performance evaluation was used to characterize the main performance parameters of the sensor alone. These parameters are conversion gain, decomposition of the three main noise sources (read, shot and fixed pattern noise), full well capacity and dynamic range [7]. Read noise is defined as any noise source that is not a function of signal. It includes any noise sources independent from the signal level, such as pixel source follower noise, sense node reset noise, thermal dark current shot noise, dark current fixed pattern noise (FPN), ADC quantizing noise, offset FPN and system noise. Shot (or primary quantum) noise arises from the Poisson distribution of the interacting optical photons, and is therefore equal to the square root of the signal at each specific level. Fixed pattern (or structure) noise is correlated noise because its pattern remains the same in repeated frames taken with the same detector. The first two types of noise have a temporal nature, while FPN is spatial. The gain FPN of a CMOS sensor describes the spatially fixed variations in the gain across the sensor. More specifically, it is related to pixel-to-pixel and column-to-column non uniformities, due to differences in sensitivity and the transistor's gain inside each pixel and differences in the gain of columns amplifiers, respectively [35]. The magnitude of the gain FPN is proportional to the signal level. Since gain FPN is not a stochastic noise contribution it needs to be removed to calculate the intrinsic SNR of the detector. All these noise contributions can be expressed in electrons root mean square (r.m.s.). The full well capacity shows the maximum electron charge that the photodiode's sense node inside each pixel can accommodate. Above this charge level saturation occurs. The dynamic range is defined by the largest signal (full well capacity of the photodiode) divided by the smallest possible signal (read noise) the detector can read.

2.2.2. Extraction of the electro-optical performance parameters

The conversion gain allows representing the detector's performance parameters in absolute units (electrons), instead of the relative digital numbers (DN) given as output by the detector. The extraction of the conversion gain by means of the mean-variance (MV) analysis has been described in detail elsewhere [7,36,37], and it can be expressed as

$$\sigma_S^2 = G\overline{S} + \sigma_R^2 \tag{1}$$

where $\sigma_R^2(DN^2)$ is the signal-independent read noise, $\sigma_S^2(DN^2)$ is the total measured temporal noise (including both signal-independent and signal dependent noises) at a given average signal level $\overline{S}(DN)$ and G is the conversion gain (in DN/e$^-$). Plotting $\sigma_S^2(DN^2)$ against $\overline{S}(DN)$ results in an MV graph. The slope of the graph provides G(DN/e$^-$), while the intercept gives $\sigma_R^2(DN^2)$. Therefore, the sensor conversion gain K(e$^-$/DN) (which is the inverse of G) can be extracted from this curve. The data for the MV graph are determined from N frames measured at a number of

homogeneous illumination levels between dark and saturation. To calculate the total measured temporal noise, the temporal variation of each pixel around its average value (over N frames) is calculated. Then, a 2D matrix with $\sigma_S^2(x,y)$ is created. The spatial average over x rows and y columns results in $\sigma_S^2(DN^2)$.

The electro-optical characterization was separately applied to each of the six parallel readout channels (1944×256 pixels each) of each sensor to extract all parameters described above, which are slightly different for each channel. In this study x was equal to 975 rows and y to 254 columns, respectively. The results were then combined (i.e. simply averaged) to obtain the average electro-optical parameters of the four sensors forming the X-ray detector. The read noise is given by the product of the r.m.s. dark noise (in DN) with the conversion gain, i.e. $\sigma_R(e^-)=K(e^-/DN)\sigma_D(DN)$. The full well capacity is given by the product of the overall signal level at which the maximum variance occurs (without subtracting the dark level) multiplied by the conversion gain, i.e. $FW(e^-)=K(e^-/DN)S_{max}(DN)$. The dynamic range is extracted from the combination of read noise and full well capacity as $DR(e^-)=20\,log(FW(e^-)/\sigma_R(e^-))$. To obtain the images used for the MV analysis, the sensor was uniformly illuminated with a light emitting diode (LED) with a peak wavelength at 530 nm (green light) and full width at half maximum (FWHM) of 20 nm. In each readout channel the used ROI covered the half (25–75%) vertical area to achieve an estimated light non-uniformity of less than 7%. The total light non-uniformity on each sensor (i.e. including all six parallel readout channels) was less than 11%. To achieve different signal levels, the pulse times of the LED were varied (between 0.1–12 ms and 0.1–3.5 ms in the HFW and LFW modes, respectively). Finally, error propagation was used to estimate the accuracy of all results.

2.3. X-ray performance evaluation

2.3.1. Beam quality

The X-ray performance evaluation was carried out using two Tungsten anode (W) X-ray tubes, the Varian RAD-70 for mammography and the Philips SRO 33/100 for general radiography. Three beam qualities were used to cover a range of different medical applications: 28 kV for mammography and 50 kV (RQA3) and 70 kV (RQA5) for general radiography according to the IEC standard [32,33]. Aluminum (Al) filtration was added externally to simulate the breast and parts of the human body respectively according to the specified beam qualities in both cases. The thickness of the Al filtration thickness was adjusted (2.3 mm (99.999% pure), 7.9 mm and 21.6 mm Al (99.99% pure)[38]) to reach the required half value layers (HVL) for each beam quality within 3% accuracy. The measurements of the HVLs were made using thin Al foils with 99% purity [39] and a calibrated ion chamber (KEITHLEY 35050A Dosimeter). According to Samei [40] RQA3 is suitable in neonatal and pediatric extremities imaging, while RQA5 is commonly used to image extremities, head and shoulder in adults. Inserting the used kV/HVL combination into a spectrum simulator software (Spektr) enabled the estimation of the fluence per exposure ratio (Φ/K_a) [41] (or ideal SNR^2 input per K_a), which is required by the DQE calculation. Spektr is a MATLAB based graphical user interface (GUI) [42] which adapts the TASMIP algorithm of Boone and Seibert [43]. Table 1 shows the required, measured and estimated values of the beams used.

2.3.2. X-ray converters

The CMOS APS sensor was optically coupled to two different Thallium-activated structured Cesium Iodide (CsI:Tl) scintillators, the choice of which depended on the beam quality used. Due to the light-guiding effect in the scintillator, this type of scintillator preserves good spatial resolution at the increased scintillator thickness necessary for appropriate X-ray stopping power [44]. A fiber optic plate (FOP) was attached to the sensor's surface to eliminate the direct absorption of X-rays in the sensor. According to Flynn et al. [45], a directly detected X-ray photon produces large charge, in the order of 4700 e^- for a 17 keV X-ray absorbed in Si. Hence, about 200 X-rays are sufficient to saturate an imager with one million e^- full well capacity, and result in significant quantum noise. A thin high resolution (HR) scintillator was used at 28 kV to preserve the spatial resolution while a thicker high light (HL) output scintillator was employed at higher energies to account for the higher penetration of the X-ray beam. The X-ray detection from a scintillator, described by the parameters quantum detection efficiency (QDE) and the energy absorption efficiency (EAE), depends on the energy of the incident X-ray photons, the material and thickness of the scintillator [46].

2.3.3. X-ray sensitivity

The X-ray sensitivity of the detector for each beam quality was expressed through the signal transfer property (STP), which is expressed as the average output in DN for a given K_a value. The average DN was calculated from the total pixel area used for the NNPS analysis (see below) from each frame over 5 frames. The images were dark field subtracted and flat field corrected to apply gain and offset correction. The K_a was measured with a calibrated ion chamber (KEITHLEY 35050A Dosimeter). Finally, a linear regression fit was applied to assess the linearity of the sensor in each case.

2.3.4. Presampling modulation transfer function (pMTF)

The pMTF describes the contrast reduction of the different spatial frequencies that compose the image, and it is used to quantify the resolution of an imaging system. It shows how efficiently an input signal is transferred to the output at each spatial frequency. For the determination of the pMTF, the edge technique [47] was used according to the IEC standard. An opaque, polished edge test object (W foil, 1 mm thick, 99.95% pure [48])

Table 1
Values related to the used beam qualities.

Parameter	Beam quality (Mammo)	Beam quality 3 (RQA3)	Beam quality 4 (RQA5)	Units
Anode/filtration combination	W/Al	W/Al	W/Al	
IEC nominal tube voltage	28	50	70	kV
Tube voltage	28	50	70	kV
IEC added filtration	2.0	10.0	21.0	mm Al
Experimental added filtration	2.3	7.9	21.6	mm Al
IEC HVL	0.83	4.0	7.1	mm Al
Measured HVL	0.82	4.0	7.1	mm Al
IEC Φ/K_a	6575	21,759	30,174	X-rays/μGy/mm^2
SPEKTR Φ/K_a	7009	22,572	30,608	X-rays/μGy/mm^2

was placed at a shallow angle α (1.5°–3°) with respect to the detector pixel rows and columns. The angle at which the edge was positioned with respect to the detector pixels rows or columns was estimated using the linear regression technique [49,50]. The pixel values of the corrected data of seven consecutive lines (i.e. rows or columns depending on the edge's orientation) centrally located across the edge were then used to generate seven oversampled edge profiles or edge spread functions (ESF). It was found that seven ESF curves are sufficient to reduce the statistical noise and simultaneously cover both the dark and white areas of the edge test image. The central ESF was detected automatically and the adjacent six ESF curves (three at each side) were selected accordingly. More than one ESF curves (i.e. seven in our case) were combined to reduce the statistical noise. An ESF was selected as the reference one, and the remaining six shifted laterally until the position overlapping most closely the reference one was reached. Two methods can be applied to optimize this lateral shift. The first one is to compare the correlation coefficient between each shifted ESF and the reference one, and select the line at which the maximum correlation is achieved. However, this method can be affected by defective pixels or lines leading to erroneous shift estimation. The second method uses the equation $N = round(1/tan\,\alpha)$ to calculate the number of lines N necessary for the edge to shift laterally by 1 pixel [32,33,51]. Both methods were tested in each case, and the one providing the highest correlation between the shifted ESF curves was used to calculate the average oversampled ESF. The sampling distance in the oversampled ESF is assumed to be constant, and is given by the pixel pitch Δx divided by N. The oversampled ESF was then differentiated to get the oversampled line spread function (LSF). Fig. 1 shows an example of the various steps from the oversampled ESF curves to the LSF. It may be observed that the noise on the right part of the LSF is higher. This happens because it scales with the signal.

The MTF was obtained from the modulus of the fast Fourier transform (FFT) of the oversampled LSF. The MTF was normalized to one at zero frequency, and then calculated until the Nyquist frequency (F_{Nyq}) to avoid noise aliasing effects, leading to pre-sampling MTF (pMTF). In accordance with the IEC standard, the horizontal and vertical pMTFs have been calculated by binning

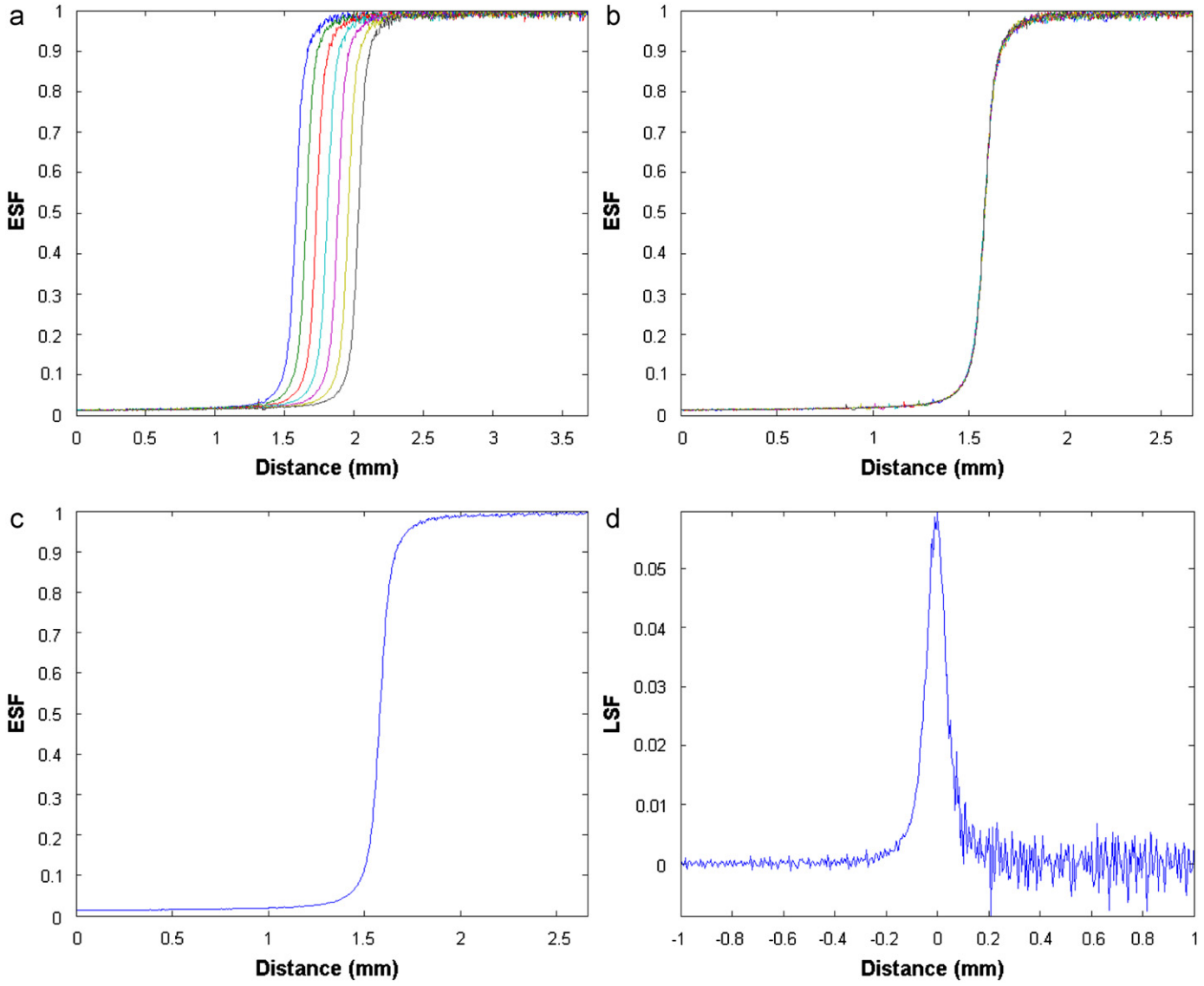

Fig. 1. A representation of the MTF calculation process – (a) oversampled ESF curves, (b) shifted oversampled ESF curves, (c) average oversample ESF curve, and (d) oversampled LSF.

the data points in a frequency interval f_{int} ($f-f_{int} \le f \le f+f_{int}$) around the spatial frequencies from 0.5 to F_{Nyq} with an interval of 0.5 lp/mm. f_{int} is obtained as $0.01/\Delta x$(mm) [32,33]. Finally, the average (over the edge's orientation) pMTF was calculated. A second order polynomial fit correction was applied on the edge test images to remove low frequency (background) trends arising from the X-ray field's non-uniformity (e.g. heel effect, etc.) that could distort the MTF at low frequencies [32,33].

2.3.5. Noise power spectrum (NPS)

The NPS describes the spectral decomposition of the noise variance in an image as a function of spatial frequency, thus expressing the noise transfer. Flat field images were acquired to calculate the noise. Offset and gain corrections were applied to the flat images to remove the dark offset and minimize gain variations between different pixels (i.e. to remove the gain FPN).

The NPS was then calculated by applying a 2D algorithm to a corrected flat field image according to the IEC standard. First, overlapping regions of interest (ROI) of 256×256 pixels were taken from a central area of the image. At least four million independent image pixels are required for an accuracy of 5% for the 2D NPS [32,33], and therefore a number of flat field images sufficient to meet this criterion was used. The entire detector was irradiated during the acquisition of flat field images. Each captured image was corrected for the presence of background trends (e.g. heel effect) by fitting a second order polynomial and subtracting the fitted 2D function $S(x, y)$ from the flat field image $I(x, y)$. This second order polynomial de-trending corrected the NPS at frequencies lower than 1 lp/mm [32,33,46]. The average 2D NPS has then been calculated by applying the following equation [32,33,46]:

$$NPS(u,v) = \frac{\Delta x \Delta y}{M N_x N_y} \sum_{m=1}^{M} \left| FFT\{I(x_i,y_i) - S(x_i,y_i)\} \right|^2 \quad (2)$$

where u and v are the spatial frequencies corresponding to x and y, Δx and Δy are the x and y pixel pitches, N_x and N_y express the ROI size in pixels in the x and y directions (256 according to the IEC), M is the number of ROIs used in the ensemble average, and FFT denotes the fast Fourier transform operation.

In order to use the NPS for the DQE calculation, one dimensional (1D) profiles were extracted from the 2D NPS. Data from seven rows and seven columns on both sides of the corresponding axis (a total of 14), omitting the axis itself, were averaged, resulting in the horizontal and vertical 1D NPS. The axes were omitted because they are susceptible to any remnant column- or row-wise gain FPN. Each data point was associated to a specific spatial frequency by means of the equation $f = \sqrt{u^2+v^2}$. As done when calculating the MTF, smoothing was obtained by averaging the data points within the 14 rows and columns that fall in a frequency interval of f_{int} around the spatial frequencies from 0.5 to F_{Nyq} with an interval of 0.5 lp/mm (see Section 2.3.4) [32,33,46].

The horizontal and vertical NPS(f) were then divided by the (large area signal)^2 to obtain the normalized NPS (NNPS), expressed in terms of relative input exposure fluctuation [46,52]. The term "large area signal" was taken to be the mean DN in the image for each particular dose: this can be obtained from the STP (after offset and gain corrections). Finally, the horizontal and vertical 1D NNPS were combined to calculate the average 1D NNPS.

2.3.6. Detective quantum efficiency (DQE)

The DQE expresses the ability of the detector to transfer the SNR from its input to its output. It quantifies the fraction of input X-ray quanta used to create an image at each spatial frequency and describes the ability of a particular system to effectively use the available input quanta. Practically, it can be calculated from the following equation [32,33,46]:

$$DQE(f) = \frac{SNR_{out}^2}{SNR_{in}^2} = \frac{MTF^2(f)}{\frac{\Phi}{K_a} \cdot K_a \cdot NNPS(f)} \quad (3)$$

The IEC standard assumes that an ideal detector behaves as an ideal photon counter [47]. Therefore, the fluence per exposure ratio Φ/K_a for each beam quality was calculated according to the following equation [42,46,47,53]:

$$\frac{\Phi}{K_a} = \int_0^{kV} \Phi_{norm}(E) \frac{WQ}{(\frac{\mu_{en}(E)}{\rho})_{air} Ee \times 10^8} dE \quad (4)$$

where $\Phi_{norm}(E)$ is the normalized spectrum, W (or W-value) is expressed in units of eV per ion pair (eV/i.p.) and the best current value for X-rays in dry air is 33.97 eV/i.p., Q is the charge liberated in air by one R (2.58×10^{-4} C/kg/R) and e is the electronic charge (1.6022×10^{-19} C). The detector studied is an energy integrating detector, so an energy-weighted calculation of the Φ/K_a would be more realistic. However, Samei and Flynn [47] found that for RQA5 beam quality (74 kV) the difference between the energy-weighed and photon-counting approximations is less than 3%. This difference is even smaller for lower kV spectra.

The product $(\Phi/K_a) \cdot K_a$ corresponds to the SNR^2 input due to the Poisson distribution of the input quanta. Therefore, the SNR^2 output is calculated from the ratio between MTF^2 and NNPS. An ideal imaging system would be characterized by a DQE equal to one at all spatial frequencies. In practice, there is always a departure from this behavior and the DQE decreases gradually with increasing spatial frequencies. This occurs due to the decreased signal transfer (pMTF) and the increased effect of the noise as a function of spatial frequency [54].

At low K_a levels the electronic noise (read noise and dark current) is comparable to the signal produced by the X-ray quanta, and may therefore have a strong effect on the overall noise (NNPS), decreasing the DQE. At this low signal level the system is defined as electronic noise limited. Also, at this level the DQE could be decreased in case of secondary quantum sink, i.e. the situation in which the number of secondary visible photons collected and detected per input X-ray photons is less than unity [45]. However this problem can usually be solved by adjusting the gain and the collection efficiency [55]. As the K_a level increases, this effect decreases and the DQE increases. Finally, at high signal levels this effect is negligible and the DQE reaches a maximum. At this level the system is quantum limited, as the performance is practically limited only by the quantum noise. One of the few cases in which the DQE may decrease at high signal levels is when there is a substantial level of gain FPN, the amplitude of which increases linearly with the signal, and therefore becomes predominant at high dose [56]. However, appropriate gain and offset corrections are normally sufficient to eliminate this effect.

All data analysis for both electro-optical and X-ray performance evaluation was made using custom software written in MATLAB version 7.10 (The MathWorks, Natick, MA, USA).

3. Results and discussions

3.1. Electro-optical evaluation

Fig. 2 shows representative MV curves for the CMOS APS in the HFW and LFW mode, respectively. The measurements were made using the full resolution mode of the sensor. x and y axes

correspond to the mean DN of the offset corrected images and to the r.m.s. noise, respectively. It can be seen that the LFW mode results in higher shot noise at a given signal level, which according to (1) corresponds to lower conversion gain $K(e^-/DN)$. A preliminary analysis of this figure shows that the full well capacity of the photodiode (i.e. the point corresponding to the maximum shot noise) is about 13,200 DN in the HFW and 11,800 DN in the LFW. However, this comparison is made in relative units (DN) rather than absolute ones (e^-). A proper comparison in terms of electrons is made in Table 2. This table shows the performance parameters of the six readout channels (operated in HFW mode) forming a CMOS sensor. After the full well capacity saturation occurs and the noise decreases because any additional signal spills over into surrounding pixels resulting in noise averaging. This happens because the photodiode cannot hold any additional electron charge.

Table 3 provides the overall performance parameters of the four sensors forming the X-ray detector. The results demonstrate the performance of the detector in both HFW and LFW modes. The conversion gain can be changed at the pixel level by switching from one mode to the other. This operation is performed globally and statically. In particular, switching from LFW to HFW mode corresponds to a 3-fold gain increase. This option enables a choice between low read noise at a lower (by a factor of three) dynamic range, or higher dynamic range with a reduced noise performance [57]. In other words, LFW mode is suitable for low K_a levels, where the electronic noise dominates, while HFW is best suited for higher exposure levels.

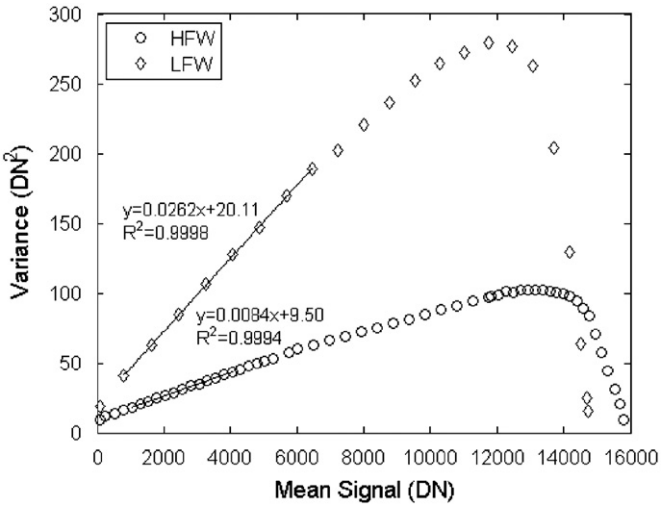

Fig. 2. Representative MV curves for HFW and LFW modes.

3.2. X-ray performance evaluation

3.2.1. X-ray sensitivity

Fig. 3 shows STP curves of the detector obtained by plotting the mean pixel value (DN) as a function of K_a at 28, 52 and 70 kV. The signal transfer of the detector was found to be reasonably linear with coefficients of determination (R^2) greater than 0.998 in all cases. It can be seen that the detector saturates at much lower K_a level when operating at the LFW mode, due to the higher conversion gain.

The mammographic exposure range (at detector's surface) used for the X-ray characterization of the detector was from 22.6 to 138.6 μGy in the HFW mode. Ranges normally found in the literature are of 100–120 μGy [46,58–60]. The IEC 62220-1-2 [32] recommends that for a complete characterization of an X-ray digital detector the exposure range should be at least between half and twice the "reference" level. The exposure level in the LFW mode was 22.6–44.7 μGy. The average detector K_a for general radiography is around 2.5 μGy [46,58–60]. The corresponding IEC standard [33] recommends that the exposure range should be at least between 1/3.2 and 3.2 times the normal level (i.e. from 0.8 to 8 μGy). We chose a wider exposure range (0.26–12.31 μGy) using HFW mode to exploit the performance of the detector within the exposure range used for general radiography [46]. A comparison between the STP curves of the detectors over the three energies (28, 52 and 70 kV) shows that the slope increases as a function of energy. This implies an increase of the output signal (in DN) per unit K_a as the mean X-ray energy increases. According to Marshall [61], this happens mainly due to three reasons. First, the number of X-rays per unit K_a per unit area (i.e. the Φ/K_a parameter) increases as the mean X-ray energy increases up to around 60 keV [46]. Therefore more

Table 2
The performance parameters of the six readout channels (operated in HFW mode) forming a CMOS sensor.

Parameter	Chan. 1	Chan. 2	Chan. 3	Chan. 4	Chan. 5	Chan. 6	Average
K (e^-/DN)	119.2 ± 0.9	120.8 ± 2.0	119.7 ± 2.3	120.2 ± 1.1	119.0 ± 2.5	119.6 ± 3.0	119.7 ± 2.1
Read noise (e^-)	366.2 ± 2.6	367.8 ± 6.2	363.1 ± 7.0	364.7 ± 3.4	352.1 ± 7.5	356.6 ± 8.9	361.7 ± 6.3
Full well capacity (e^-)	$(1.58 \pm 0.01) \times 10^6$	$(1.59 \pm 0.03) \times 10^6$	$(1.56 \pm 0.03) \times 10^6$	$(1.62 \pm 0.02) \times 10^6$	$(1.52 \pm 0.03) \times 10^6$	$(1.59 \pm 0.04) \times 10^6$	$(1.58 \pm 0.03) \times 10^6$
Dynamic range (dB)	72.7 ± 0.2	72.7 ± 0.5	72.7 ± 0.5	72.9 ± 0.3	72.7 ± 0.6	73.0 ± 0.7	72.8 ± 0.5

Table 3
Summary of the performance parameters of the four sensors forming the X-ray detector.

Parameter (1 × 1 mode)	HFW mode	LFW mode	Units
Conversion gain K	119.6 ± 2.9	38.8 ± 0.6	e^-/DN
Read noise	361.9 ± 8.7	164.9 ± 2.6	e^-
Full well capacity	$(1.57 \pm 0.04) \times 10^6$	$(4.58 \pm 0.07) \times 10^5$	e^-
Dynamic range	72.8 ± 0.7	68.9 ± 0.4	dB

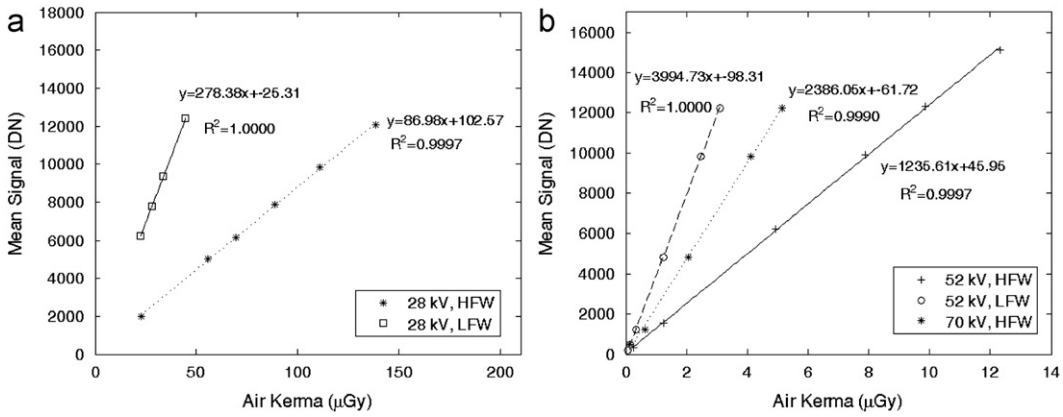

Fig. 3. STP curves with fitting function equations displayed at (a) 28 kV and (b) 52 kV and 70 kV.

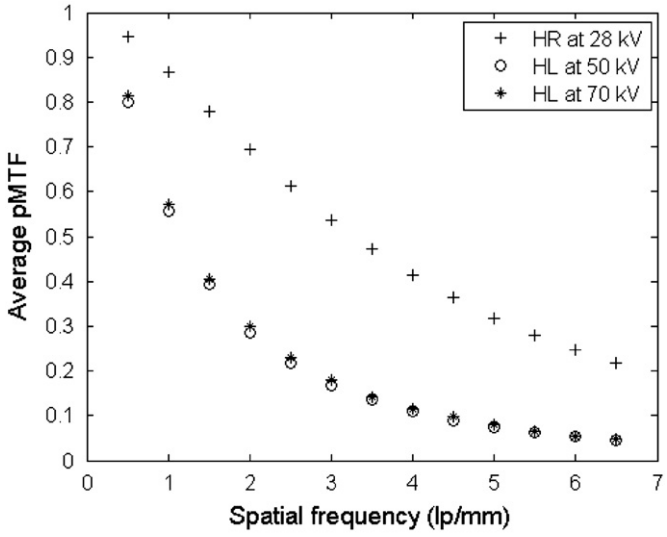

Fig. 4. Average pMTFs at 28, 50 and 70 kV using two thicknesses of CsI:Tl scintillator.

X-rays that are signal carriers are impinging the scintillator per unit K_a. Secondly, more secondary quanta (light photons for scintillators and electronic charge for photoconductors) are generated assuming a fixed conversion efficiency (i.e. light yield for scintillator). Finally, there is a depth effect, which can be explained as follows. As the mean energy increases the beam becomes more penetrating, so the interacting X-rays are absorbed at deeper points within the scintillator, closer to the digital sensor. Hence, the created optical photons are reabsorbed less from the scintillator. This increases their collection efficiency from the digital sensor.

3.2.2. Spatial resolution (signal transfer)

Fig. 4 illustrates the pMTF curves at different energies. For mammographic conditions, the detector's pMTF reaches 50% at about 3.3 lp/mm for the 28 kV beam quality. At higher energies, the use of the thicker scintillator results in a trade-off between X-ray sensitivity and resolution compared to the thin one. The decreased resolution can clearly be appreciated in the figure. Both beam qualities result in almost identical resolution. The pMTF reaches 50% at 1.2 lp/mm for 50 kV and 70 kV. These values are in good agreement with the results of the pMTF measurements on similar systems previously reported in the literature [62–65] (see Table 4). The pMTF at 28 kV has a moderate residual value (around 20%) at the Nyquist frequency, which is in our case 6.7 lp/mm. Thus, an amount of high-frequency signal beyond the Nyquist frequency (i.e. spatial size less than 150 μm) may be aliased by the detector [56]. Aliasing is reduced when the thick (HL) scintillator is used, due to the decreased resolution (10% pMTF level at around 4.5 lp/mm). All pMTF curves were calculated from edge test images acquired at approximately half saturation levels. According to the literature [40] the sharpness of digital detectors is usually not dependent on exposure. However, a relatively high exposure level is required to reduce the level of noise in the measurement.

3.2.3. Noise assessment (noise transfer)

The 1D NNPS is required by the DQE calculation and gives information about the noise response of the detector. For brevity's sake, only the NNPS curves at 28 kV for both HFW and LFW modes are shown (Fig. 5). The NNPS data in the HFW mode are represented with markers only, while the respective in the LFW mode are shown with dashed lines plus markers. It can be seen that NNPS values depend on exposure and decrease with K_a. This happens due to the larger increase in the signal compared to the increase in noise, and results in increased DQE values as a function of exposure. We can see that for a given K_a level (22.6 μGy) the NNPS values are similar in both modes. As specified in the IEC standard, since the 1D NNPS were calculated from more than four million independent pixels, an accuracy of at least 5% is obtained.

3.2.4. DQE (SNR^2 transfer)

Fig. 6 illustrates the DQE as a function of spatial frequency at 28 kV. The DQE(0.5) values range from 0.65 to 0.69 in the HFW mode and from 0.66 to 0.66 in the LFW mode, respectively. The maximum K_a levels for both full well modes were selected to avoid saturation of the photodiode, as this would result in artificially high DQE values due to a decrease in the measured r.m.s. noise compared to the mean signal (see Fig. 2). There were no significant differences between the DQE values along the horizontal and vertical axis of the detector. The DQE curves have comparable shapes for all exposure levels evaluated, as the frequency composition of the DQE does not depend on the exposure [56].

A review of the literature indicates that this detector compares well with other flat panel detectors as demonstrated by the main parameters summarized in Table 4 [62–65]. All characterization

Table 4
Comparison of physical parameters of different mammographic systems.

System	FUJIFILM [62]	Sectra [63]	Fischer [64]	General electric [64]	Hologic [65]	Dexela
	AMULET	*MicroDose*	*Senoscan*	*Senographe 2000D*	*Lorad Selenia*	*2923*
Detector technology	Direct flat panel	Direct photon counting	CCD	Indirect flat panel	Direct flat panel	CMOS APS
Scintillator/semiconductor material	a-Se	Crystalline Si wafer	CsI	CsI:Tl	a-Se	CsI:Tl
Radiation quality	W/Rh (28 kV)	W/Al (28 kV)	W/Al (28 kV)	Mo/Mo (28 kV)—RQA-M 2	Mo/Mo (28 kV)—RQA-M 2	W/Al (28 kV)
pMTF (50%) (*x*; *y* direction)	4.4	6.2; 3.3	5.5	4	5.8	3.3
DQE peak (*x*; *y* direction) at average exposure level	0.75at 103 μGy	0.63; 0.61 at 113 μGy	0.24 at 131 μGy	0.53 at 131 μGy	0.59 at 92.5 μGy	0.68 (HFW) at 111 μGy

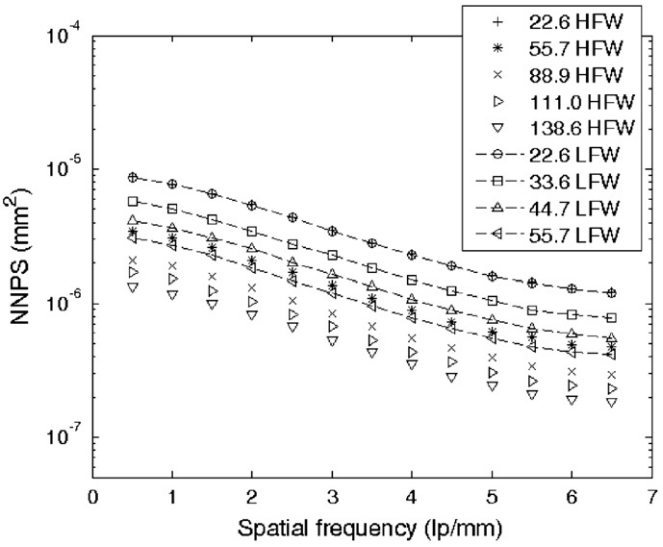

Fig. 5. 1D NNPS at different values of K_a at 28 kV for both full well modes.

measurements were made according to the IEC 62220-1-2 [33]. However, there are some differences in the beam quality (anode/filtration combination and energy used), experimental conditions, type and thickness of the detecting material (scintillator or semiconducting material) and data processing which may affect the results. In order to eliminate these differences, the performance of the CMOS X-ray detector under investigation has been constantly compared to W/Al or W/Rh combinations at 28 kV, which are broadly used in mammography, with the exception of GE Senographe 200D and Hologic Lorad Selenia systems (Mo/Mo at 28 kV). To the best of our knowledge, no one has characterized these detectors using W/Al combination for mammographic conditions yet.

Table 4 shows that the spatial resolution of the investigated CMOS X-ray detector is slightly lower compared to the other systems. However, it has high DQE value at 0.5 lp/mm. According to Saunders et al. 2009 [66], a small reduction in spatial resolution has moderate impact on the system's diagnostic performance. On the other hand, increased quantum noise substantially limits the detectability of fine-details such as microcalcifications as well as the discrimination between benign and malignant masses. The performance of the system is therefore effectively described by means of the contrast-detail resolution, which at a given dose is driven by the DQE, as systems with higher DQE will reach the same contrast-detail resolution at a lower dose [67]. Figs. 4 and 6 indicate that the studied detector can detect fine-details down to 150 μm without aliasing. The limit of microcalcifications detectability in overview (unmagnified) digital mammographic systems is still considered to be 130 μm [68]. Hence, there are no prominent limitations to the use of this detector in Mammography.

Fig. 7 presents the DQE as a function of spatial frequency for RQA3 and RQA5 beam qualities. The DQE(0.5) values for the first beam quality range from 0.58 to 0.71 (over the considered exposure range) in the HFW mode and from 0.53 to 0.70 in the LFW mode, respectively. Concerning the RQA5 beam quality, the DQE(0.5) values range from 0.69 to 0.75 in the HFW mode. In this case we have deliberately introduced two much lower exposure levels to explore a region of the sensor where electronic noise dominates and therefore the detector is not quantum limited. However, as it can be seen from all other exposure levels, the sensor quickly reaches quantum limited behavior for exposure levels commonly used.

Table 5 provides a list of performance characteristics for six general radiography systems [69]. Compared to other systems, the investigated detector shows comparable spatial resolution and high DQE. These results indicate high potential for use under general radiography conditions.

4. Conclusions

The purpose of this study was to perform a complete evaluation of the electro-optical and X-ray performance of a CMOS X-ray detector flexibly designed for mammography, breast tomosynthesis and general radiography applications. For the electro-optical characterization, the MV analysis was used to measure the performance parameters. The results quantified the trade-off between electronic noise and dynamic range that the capability to switch between two different full well modes offers. For the X-ray characterization, the following parameters were extracted: X-ray sensitivity, pMTF, NPS and DQE. The detector was optically coupled to two structured CsI:Tl scintillators of different thickness and evaluated under mammographic and general radiography conditions, respectively. The HFW mode DQE values from this study were compared to those of other mammographic systems, obtained under similar experimental conditions. The results showed that the detector meets the requirements for mammographic examinations. The study was also extended to general radiography conditions under RQA3 and RQA5 beam qualities. The HFW DQE values with the RQA5 beam were compared to those of other general radiography systems, obtained under the same beam quality. The comparison showed that, upon coupling with the appropriate scintillator, the detector demonstrates high performance levels also at higher energies.

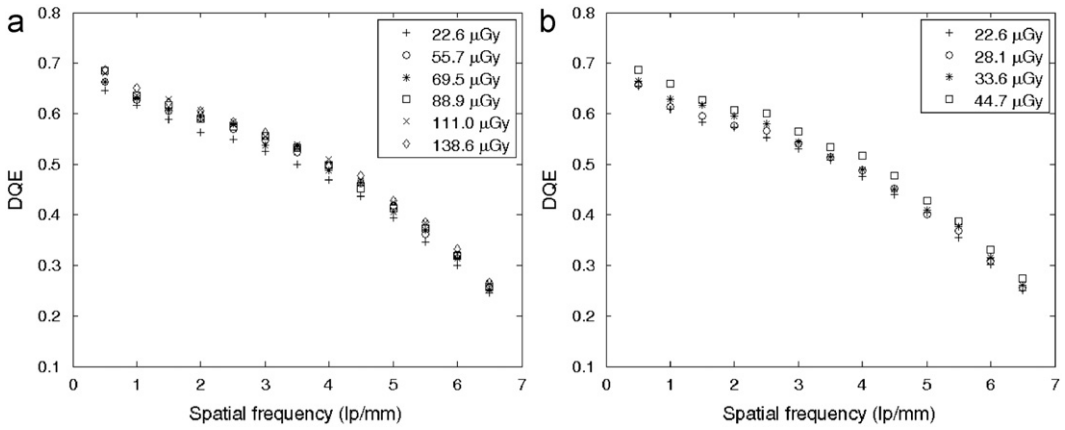

Fig. 6. DQE at 28 kV in (a) HFW and (b) LFW modes.

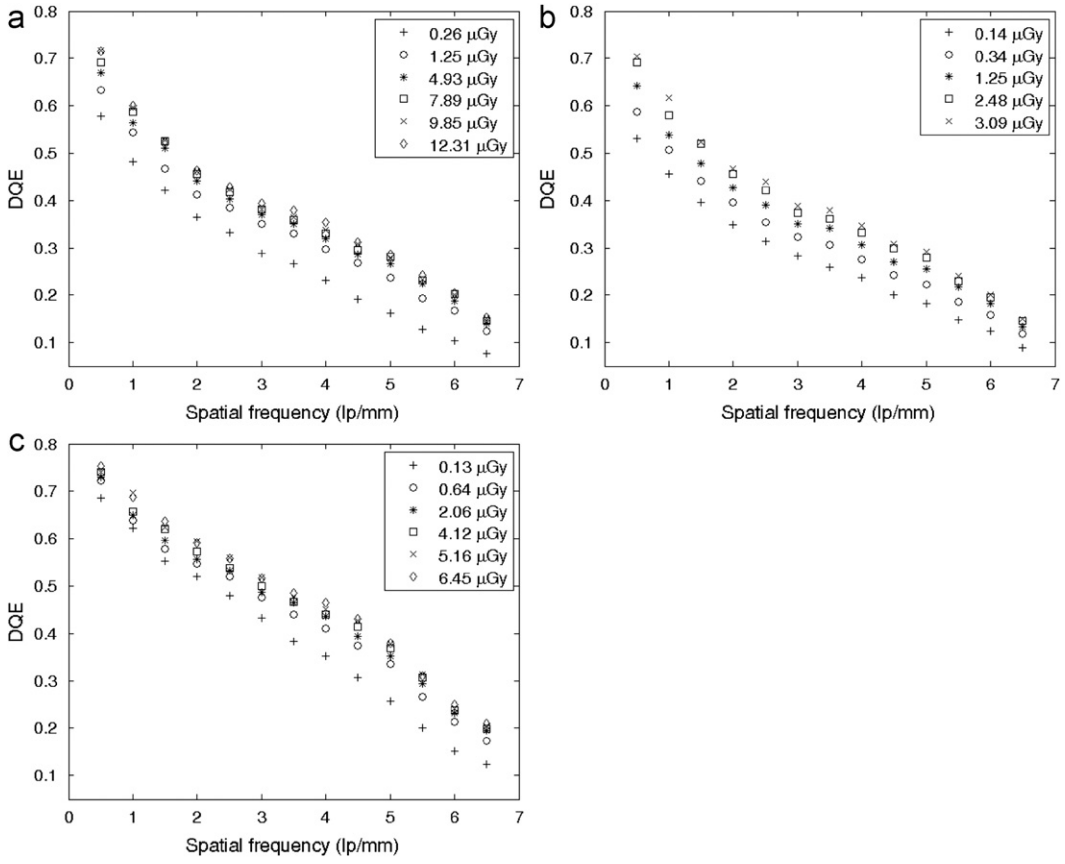

Fig. 7. DQE at 50 kV (RQA3) in (a) HFW and (b) LFW modes and at (c) 70 kV (RQA5) in HFW mode.

Table 5
Comparison of physical parameters of different systems used in general radiography.

System	**Delft** [68]	**GE** [68]	**Hologic** [68]	**SwissRay** [68]	**Trixell** [68]	**Dexela**
	ThoraScan	*Revolution*	*DirectRay*	*dOd*	*Pixium4600*	*2923*
Detector Technology	CCD	Indirect flat panel	Direct flat panel	CCD	Indirect flat panel	CMOS APS
Scintillator/semiconductor material	CsI:Tl	CsI	a-Se	CsI:Tl	CsI:Tl	CsI:Tl
Beam quality	RQA5 (70 kV)	RQA5 (70 kV)	RQA5 (70 kV)	RQA5 (70 kV)	RQA5 (70 kV)	RQA5 (70 kV)
pMTF (50%)	1.3	1.4	4.2	1.4	1.4	1.2
DQE peak at specific K_a level	0.43 at 4 μGy	0.61 at 4 μGy	0.39 at 4 μGy	0.39 at 4 μGy	0.63 at 4 μGy	0.74 (HFW) at 4.1 μGy

Acknowledgments

A.C. Konstantinidis was supported by the Greek State Scholarships Foundation (IKY). M.B. Szafraniec is partially funded by an EPSRC-GB doctoral training allowance. A. Olivo is supported by the UK Engineering and Physical Sciences Research Council (Grants EP/G004250/1 and EP/I021884/1). The detector was supported by Dexela Limited (a PerkinElmer company).

References

[1] T. Graeve, G.P. Weckler, Proceedings of SPIE 4320 (2001) 68.
[2] H.K. Kim, G. Cho, S.W. Lee, Y.H. Shin, H.S. Cho, IEEE Transactions on Electron Devices 48 (2001) 662.
[3] Q.R. Zhang, Y.H. Li, B. Steele, X.Z. Wu, W.R. Chen, J. Rong, H. Liu, Journal of Electronic Imaging 14 (2005) 1.
[4] C.D. Arvanitis, S.E. Bohndiek, G. Royle, A. Blue, H.X. Liang, A. Clark, M. Prydderch, R. Turchetta, R. Speller, Medical Physics 34 (2007) 4612.
[5] I.A. Elbakri, B.J. McIntosh, D.W. Rickey, Physics in Medicine and Biology 54 (2009) 1743.
[6] S. Mendis, S.E. Kemeny, E.R. Fossum, IEEE Transactions on Electron Devices 41 (1994) 452.
[7] D.W. Holdsworth, R.K. Gerson, A. Fenster, Medical Physics 17 (1990) 876.
[8] S. Hejazi, D.P. Trauernicht, Medical Physics 24 (1997) 287.
[9] D.S. Evans, A. Workman, M. Payne, Physics in Medicine and Biology 47 (2002) 117.
[10] L.E. Antonuk, J. Boudry, W. Wang, D. McShan, E.J. Morton, J. Yorkston, R.A. Street, Medical Physics 19 (1992) 1455.
[11] M.J. Yaffe, J.A. Rowlands, Physics in Medicine and Biology 42 (1997) 1.
[12] M. Spahn, European Radiology 15 (2005) 1934.
[13] S.E. Bohndiek, E.J. Cook, C.D. Arvanitis, A. Olivo, G.J. Royle, A.T. Clark, M.L. Prydderch, R. Turchetta, R.D. Speller, Physics in Medicine and Biology 53 (2008) 655.
[14] M.B. Williams, P.U. Simoni, Medical Physics 26 (1999) 2273.
[15] J.R. Janesick, Scientific Charge Coupled Devices, SPIE, Philadelphia, 2001.
[16] J.R. Janesick, Journal of Optical. Engineering 41 (2002) 1203.
[17] J.H. Siewerdsen, L.A. Antonuk, Y. El-Mohri, W. Huang, J.M. Boudry, I.A. Cunningham, Medical Physics 24 (1997) 71.
[18] L.E. Antonuk, K.-W. Jee, Y. El-Mohri, M. Maolinbay, S. Nassif, X. Rong, Q. Zhao, J.H. Siewerdsen, R.A. Street, K.S. Shah, Medical Physics 27 (2000) 289.
[19] W. Zhao, J.A. Rowlands, Medical Physics 24 (1997) 1819.
[20] F. Busse, W. Rutten, B. Sandkamp, P.L. Alving, R.J.M. Bastiaens, T. Ducourant, Proceedings of SPIE 4682 (2002) 819.
[21] K.W. Jee, L.A. Antonuk, Y. El-Mohri, Q. Zhao, Medical Physics 30 (2003) 1874.
[22] D. Scheffer, Proceedings of SPIE 65100 (2007) 65100O-1.
[23] J.H. Siewerdsen, D.A. Jaffray, Medical Physics 26 (1999) 1624.
[24] A.K. Bloomquist, M.J. Yaffe, G.E. Mawdsley, D.M. Hunter, Medical Physics 33 (2006) 2998.
[25] L. Korthout, D. Verbugt, J. Timpert, A. Mierop, W. de Haan, W. Maes, J. de Meulmeester, W. Muhammad, B. Dillen, H. Stoldt, I. Peters, E. Fox, DALSA Professional Imaging, 2009.
[26] R. Reshef, T. Leitner, S. Alfassi, E. Sarig, N. Golan, O. Berman, A. Fenigstein H. Wolf, G. Hevel, S. Vilan, A. Lahav, in: Proceedings of the International Image Sensor Workshop, 2009, p. 1.
[27] E.S. Said, T.Y. Chan, E.R. Fossum, R.H. Tsai, R. Spagnuolo, J. Deily, W.B. Byers Jr., J.C. Peden, IEEE Transactions on Nuclear Science 48 (2001) 1796.
[28] J. Bogaerts, B. Dierickx, G. Meynants, D. Uwaerts, IEEE Transactions on Electron Devices 50 (2003) 84.
[29] E.R. Fossum, IEEE Transactions on Electron Devices 44 (1997) 1689.
[30] A.I. Krymski, N.E. Bock, N. Tu, D. Van Blerkom, E.R. Fossum, IEEE Transactions on Electron Devices 50 (2003) 130.
[31] Dexela - CMOS X-ray detectors. Available from: 〈www.dexela.com〉.
[32] International Electrotechnical Commission Publication (IEC 62220-1), Medical Electrical Equipment—Characteristics of Digital X-ray Imaging Devices—Part 1: Determination of the Detective Quantum Efficiency, IEC, Geneva, 2003.
[33] International Electrotechnical Commission Publication (IEC 62220-1), Medical Electrical Equipment—Characteristics of Digital X-ray Imaging Devices: Part 1–2. Determination of the Detective Quantum Efficiency—Detectors Used in Mammography, IEC, Geneva, 2007.
[34] A. El Gamal, H. Eltoukhy, IEEE Circuits and Devices Magazine 21 (2005) 6.
[35] A. El Gamal, B. Fowler, H. Min, X. Liu, Proceedings of SPIE 3301 (1998) 168.
[36] L. Mortara, A. Fowler, Proceedings of SPIE 290 (1981) 28.
[37] G.R. Sims, M.B. Denton, Optical Engineering 26 (1987) 1008.
[38] NewMet - New Metals and Chemicals. Available from: 〈http://www.newmetalsandchemicals.com/default.asp〉.
[39] Goodfellow Corporation, Devon PA. Available from: 〈www.goodfellow.com〉.
[40] E. Samei, Proceedings of RSNA (2003) 37.
[41] H.E. Johns, J.R. Cunningham, The Physics of Radiology, fourth ed., Charles C. Thomas, Springfield, 1983.
[42] J.H. Siewerdsen, A.M. Waese, S. Richard, D. Jaffray, Medical Physics 31 (2004) 3057.
[43] J.M. Boone, J.A. Seibert, Medical Physics 24 (1997) 1661.
[44] V.V. Nagarkar, T.K. Gupta, S.R. Miller, Y. Klugerman, M.R. Squillante, G. Entine, IEEE Transactions on Nuclear Science 45 (1998) 492.
[45] M.J. Flynn, S.M. Hames, S.J. Wilderman, J.J. Ciarelli, IEEE Transactions on Nuclear Science 43 (1996) 2320.
[46] J. Beutel, H.L. Kundel, R.L. Van Metter (Eds.), Physics and Psychophysics, 1, SPIE, Bellingham, 2000.
[47] E. Samei, M. Flynn, Medical Physics 29 (2002) 447.
[48] Alfa Aesar - A Jonhson Matthey Company. Available from: 〈www.alfa.com〉.
[49] P.B. Greer, T. van Doorn, Medical Physics 27 (2000) 2048.
[50] B.D. Price, C.J. Esbrand, A. Olivo, A.P. Gibson, J.C. Hebden, R.D. Speller, Rev. Sci. Instrum. 79 (2008) 113103-1.
[51] E. Buhr, S. Gunther-Kohfahl, U. Neitzel, Medical Physics 30 (2003) 2323.
[52] J.C. Dainty, R. Shaw, Image Science—Principles, Analysis and Evaluation of Photographic-type Imaging Processes, Academic Press Inc., London, 1974.
[53] J.M. Boone, Proceedings of SPIE 3336 (1998) 592.
[54] M.B. Williams, E.A. Krupinski, K.J. Strauss, W.K. Breeden III, M.S. Rzeszotarski, K. Applegate, M. Wyattg, S. Bjork, J.A. Seibert, Journal of the American College of Radiology 4 (2007) 371.
[55] E.D. Pisano, M.J. Yaffe, C.M. Kuzmiak (Eds.), Digital Mammography, Lippincott Williams and Wilkins, Philadelphia, 2004.
[56] P. Monnin, D. Gutierrez, S. Bulling, D. Guntern, F.R. Verdun, Medical Physics 34 (2007) 906.
[57] S. Naday, E.F. Bullard, S. Gunn, J.E. Brodrick, E.O. O'Tuairisg, A. McArthur, H. Amin, M.B. Williams, P.G. Judy, A. Konstantinidis, Proceedings of IWDM 6136 (2010) 428.
[58] K.-W. Jee, L.E. Antonuk, Y. El-Mohri, Q. Zhao, Medical Physics 30 (2003) 1874.
[59] C. Ghetti, A. Borrini, O. Ortenzia, R. Rossi, P.L. Ordóñez, Medical Physics 35 (2008) 456.
[60] J.P. Moy, Nuclear Instruments and Methods in Physics Research Section A 442 (2000) 26.
[61] N.W. Marshall, Physics in Medicine and Biology 54 (2009) 2845.
[62] S. Rivetti, N. Lanconelli, M. Bertolini, G. Borasi, P. Golinelli, D. Acchiappati, E. Gallo, Medical Physics 36 (2009) 5139.
[63] I. Honey, C. Lawinski, P. Blake, A. Mackenzie, H. Cole, D. Emerton, Report 06045: Full Field Digital Mammography Systems Sectra MicroDose—A Technical Report, Centre for Evidence-based Purchasing (CEP), London, 2006.
[64] B. Lazzari, G. Belli, C. Gori, M. Rosselli Del Turco, Medical Physics 34 (2007) 2730.
[65] P. Blake, C. Lawinski, A. Mackenzie, I. Honey, H. Cole, D. Emerton, Report 05084: Full Field Digital Mammography Systems Hologic Selenia—A technical report, Centre for Evidence-based Purchasing (CEP), London, 2006.
[66] R.S. Saunders Jr., J.A. Baker, D.M. Delong, J.P. Johnson, E. Samei, Medical Physics 36 (2009) 5139.
[67] U. Bick, F. Diekmann, European Radiology 17 (2007) 1931.
[68] U. Bick, F. Diekmann (Eds.), Digital Mammography, Springer, Berlin, 2010.
[69] C. Lawinski, A. Mackenzie, H. Cole, P. Blake, I. Honey, Report 05078: Digital imaging systems for general radiography—A Comparative Technical Report, Centre for Evidence-based Purchasing (CEP), London, 2005.